2023

The Role of Oxygen Impurities in γ-phase Calcium Lanthanum Sulfide for Infrared Applications

Alexandros Kostogiannes
University of Central Florida

THE ROLE OF OXYGEN IMPURITIES IN γ-PHASE CALCIUM LANTHANUM SULFIDE FOR INFRARED APPLICATIONS

by

ALEXANDROS KOSTOGIANNES
B.S. University of Central Florida, 2021

A thesis submitted in partial fulfillment of the requirements
for the degree of Master of Science
in the Department of Materials Science and Engineering
in the College of Engineering and Computer Science
at the University of Central Florida
Orlando, Florida

Fall Term
2023

Major Professor: Kathleen A. Richardson

ABSTRACT

Calcium lanthanum sulfide (CLS) has been identified as a candidate material for various optical applications due to its wide transmission range, high refractive index, desirable thermo-optic properties, and refractory behavior. Implementation of CLS in optical systems has remained unrealized due to various difficulties in the synthesis and bulk fabrication of this material. The key challenge facing the development of CLS is the incorporation of oxygen and the presence of unwanted secondary phases related to the lack of control of stoichiometric variations across the ternary phase diagram. Though these difficulties have been previously discussed in the processing of CLS, the exact form, mechanisms of formation and impact of these attributes have not been systematically evaluated. Each of these problems must be meticulously elaborated upon to understand what processing conditions are needed to avoid these common pitfalls which have been shown to degrade the ultimate optical quality of the resulting ceramic. This thesis investigated the role of oxygen in CLS ceramics as it applies to the resulting optical quality of the processed ceramic.

The research done specifically examined ceramic materials with high La- content, prepared by hot pressing and hot isostatic pressing. The materials chosen for this work displayed varying levels of optical quality and phase purity. Determination of the desired cubic crystal structure as the main phase present was confirmed using x-ray diffraction and transmission electron microscopy. Through the correlation of data from multiple material metrology tools, the concentration and bond environment of oxygen in the ceramics and starting powders has been determined. It has been shown that the role of oxygen does not necessarily induce local phase transformation in the crystalline material, but rather can be dissolved into the CLS crystal lattice in low levels. Raman spectroscopy has been identified as a simple, useful tool that can be used to aid future synthesis routes due to its ability to differentiate the different types of O present. This thesis demonstrates how low levels of oxygen impurities can be incorporated into the CLS lattice utilizing simple IR and Raman spectroscopy techniques.

This work is dedicated to my father, Tony.

ACKNOWLEDGMENTS

I would like to first thank my two thesis advisors, Drs. Kathleen Richardson, and Romain Gaume at the University of Central Florida. Both were invaluable as they provided the knowledge, structure, and understanding needed for me to become a worthy materials scientist. Next, I thank all my colleagues working in the Optical Materials Laboratory alongside me throughout my time here. Everyone has been very kind and helpful to me, even though I tend to break things. I am also grateful for my family and my girlfriend for all their loving support throughout this degree.

.

TABLE OF CONTENTS

LIST OF FIGURES

LIST OF TABLES

LIST OF ABBREVIATIONS

CLS – Calcium Lanthanum Sulfide

CIP – Cold Isostatic Press

CUP – Cold Uniaxial Press

DOS – Density of States

EDS – Energy Dispersive x-ray Spectroscopy

FT-IR – Fourier Transform Infrared Spectroscopy

HAADF – High Angular Annular Dark Field

HR – TEM – High Resolution Transmission Electron Microscopy

HIP – Hot Isostatic Press

HP – Hot Press

IR – Infrared

LWIR – Longwave Infrared

MCF – Materials Characterization Facility

MIR – Midwave Infared

PV – Peak to Valley

RE – Rare Earth

RMS – Root Mean Square

S / TEM – Scanning / Transmission Electron Microscopy

SAED – Selective Area Electron Diffraction

UHP – Ultra high Purity

WLI – White Light Interferometry

XRD – X-ray Diffraction

XPS – X-ray Photoelectron Spectroscopy

CHAPTER ONE: INTRODUCTION

Optical media to be used as window material for thermal imaging devices for in the infrared (IR) spectral range, between1-12 μm, must meet a variety of criteria, most importantly, good spectral transmittance combined with low loss (absorption and scatter) and for more advanced applications at higher temperatures, good thermo-mechanical properties, and low emissivity [1]. While chalcogenide glasses based on non-oxide elements have been shown to be robust candidates for bulk, planar and fiber applications in the infrared due to their compositional tailorability and scalability to a variety of sizes and geometries, crystalline solids, either single or polycrystalline, and more recently, transparent IR ceramics that are cubic in nature offer more thermo-mechanical robustness than glasses cannot offer [2]. Ceramic materials for optical applications are often cubic crystal structures as their isotropic light matter interactions avoid the scattering effects due to birefringence [2]. Materials with the diamond-body center cubic crystal structure, such as ZnS, ZnSe, Ge, CdTe, are currently among the most well-known and applied chalcogenide crystals. During the search for new cubic chalcogenide crystals in the early to mid-20th century, rare earth (RE) chalcogenides with the thorium phosphide (Th_3P_4) structure were first identified by Zachariasen during his extensive studies on the lanthanides and actinides [3, 4]. Since, this type of chalcogenide material (denoted as the γ-phase) has been investigated extensively for their thermoelectric, photocatalytic, refractory, and superconducting properties as well as their high refractive index and transparency in the mid- to long- wave IR spectral region [5-8]. In the case of lanthanum trisulfide, La_2S_3, the conversion to the cubic γ-phase occurs at high temperature (>1000 °C) and is reported to be unstable at lower temperatures [7]. This difficultly during synthesis led to the discovery that incorporation of divalent alkaline earth metals can stabilize the γ-phase at lower temperatures (as seen in the case of such compounds as $SrLa_2S_4, BaLa_2S_4, CaLa_2S_4$)[9]. Alkaline earth metal sulfides, MS (where M = Ca, Sr, and Ba) form continuous solid solutions with cubic $\gamma - La_2S_3$ from La_2S_3 to MLa_2S_4. Stoichiometric $CaLa_2S_4$(CLS) has been extensively studied throughout its range of composition [10, 11]. Depending on the concentration of Ca^{2+} the crystal structure ranges in its number of structural cation vacancies where 1 in every 9 metal

sites are vacant in pure $\gamma - La_2S_3$ to 0 vacancies at $CaLa_2S_4$ [4, 12]. Though this complete solution allows for interesting control of composition, like the other chalcogenide materials there remain challenges during fabrication at some stoichiometric compositions. Control over the metal cation to anion ration ($La{:}S$) has been shown to create difficulties in CLS due to the formation of color centers during the fabrication to transparent ceramics [8]. An added issue lies in the fact that it has been long recognized that the structures of La_2S_3 and La_3S_4 exist as a continuous solid solution such that both compounds are isostructural to each other, adopting a Th_3P_4 structure [4]. La_2S_3 is electrically insulating owing to its vacancy concentration of 1/9 of the metal sites, while stoichiometric La_3S_4 is electrically conductive and contains zero vacancies [4, 13]. However, the primary challenge that most directly impact optical quality however involves undesired oxygen contamination [10, 14]. Oxygen contamination is a well-known phenomenon that continues to plague the advancement of CLS fabrication [15]. The presence of oxygen has been generally accepted to cause the common IR absorptions in the transparent spectral region between 5 and 15 μm and to induce phase changes to lower symmetry precipitants such as the tetragonal β-La_2S_3 phase ($La_{10}OS_{14}$) which is stabilized by small amounts of oxygen [16, 17]. Descriptions in literature of oxygen (O) impurities do not fully address its structural role and impact on the optically desired γ-CLS crystal structure. γ-CLS has a complex cubic crystal structure that can accommodate a large range of metal to sulfur ratios, that dictates the optical, mechanical, and physical properties of the material [18]. While a solid solution has been shown to range between $CaLa_2S_4$ and La_2S_3 range, this study focused on the 90:10 La_2S_3:CaS composition [18]. Shown below in figure 3 is a visualization of the Th_3P_4 type crystal structure of CLS, along with the coordination of S around a given cation site which may be occupied by cations La^{3+}, Ca^{2+}, or a vacancy, *V*. Volatilization of S is known to be an issue during the synthesis and sintering of CLS. To combat this in prior efforts, a partial pressure of S is created by flowing H_2S over the reactants or powder compact [7, 19]. Furthermore, impurities (primarily oxygen) will likely influence the structural parameters if present in significant concentrations.

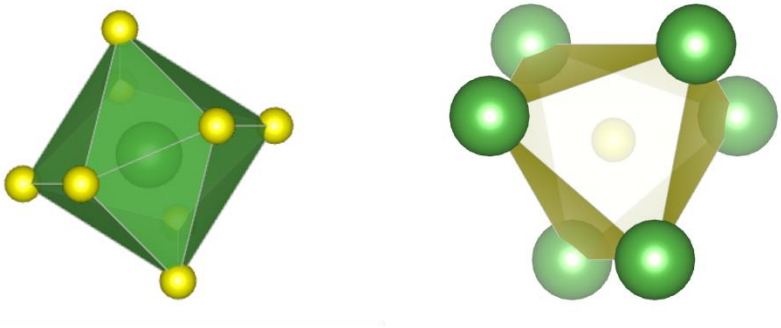

Figure 1 Visualization of cation (left) and anion sites in CLS crystal. The yellow spheres represent S and the green spheres represent La (or Ca). The Wyckoff positions for the cation sites (La, Ca, or Vac) are equivalent and randomly distributed over 12a and S occupies 16c sites. The point group associated with CLS is T_d.

Various densification and post processing techniques have been employed to combat these issues such as pressure-less sintering, spark-plasma sintering (SPS), and hot pressing (HP) as well as annealing under H_2S or CS_2 and with CLS powder in sealed quartz ampoule [8, 10, 20]. The discussion here will review previous approaches to fabricating CLS type materials to highlight the key scientific challenges that form the basis of this thesis.

Literature Review

Interest in developing CLS as an optical ceramic stems from its desirable optical, thermal, and mechanical properties [18, 21, 22]. CLS has a high melting point (1800°C) capable of transmitting light in the mid-IR (MIR)- to long-wave IR (LWIR) region (5-15 μm) and has a hardness that is double that of ZnS [18]. In addition, its interesting thermoelectric properties has made CLS a relevant material for renewable energy generation [6]. There has been significant work done to enhance the maximum transmission of CLS throughout the near half-decade of research [8, 16]. This is in part due to the work done in identifying viable routes towards the creation of a phase pure CLS material [16, 23]. Contributions from various groups have

identified key processing parameters to achieve this high level of purity [8, 16]. Further, in Durand's thesis, he utilized a simple, effective characterization tool to determine oxygen concentration in the synthesized powders to determine the most effective synthesis [16]. Table 1 summarizes his O quantification across the three different synthesis routes that he attempted using heterogenous precipitates, carbonates, and combustion methods [16]. Early work has also given indication as to where oxygen may be located within

Table 1 O quantification of $CaLa_2S_4$ powders using various synthesis techniques from Durand [16].

Method	O (wt%)
Heterogenous Precipitation	2.2
Carbonates	0.4
Combustion	0.025

the CLS structure. Systematic studies done by Besancon showed that O stabilizes one of the three allotropic variations of CLS – the tetragonal β- phase ($La_{10}OS_{14}$) – which has been an unwanted by-product of the CLS synthesis [14, 17]. These reports of oxygen are by no means exhaustive, however, they do provide a starting point for subsequent investigations of oxygen to be done. It is likely that the residual oxygen concentration seen in CLS is a result of an incomplete reaction during the powder synthesis because oxides of Ca and La are most often used as precursor compounds for sulfidation. CLS powder synthesis techniques typically involve taking salts of La and Ca, dissolving them in solution followed by a precipitation into more reactive precursor salts (carbonates, nitrates, etc.) [14, 23]. These precursor oxide materials are then fired in a furnace in an H_2S atmosphere for up to several days to convert the intimate mixture of oxide powders into the cubic sulfide [14]. In addition to the issue of extrinsic impurities in the starting material, incomplete phase conversion to the cubic γ- phase has also been reported, such that species of CaS or $\beta - CLS$ after sulfidation remain [8, 16, 23]. Table 1 summarizes the various methods by which CLS has been processed in prior efforts, and outlines some of the key attributes of powder and ceramics resulting from processing of those powders. Although it may seem intuitive to replace these conventional starting oxide

materials with oxygen free compounds such as organometallics, or pure La and Ca metals, these routes do not provide the scalability that is needed for CLS to be commercially implemented. To fabricate CLS to the scale that is needed, it seems imperative to use these oxide-based precursors with a firm understanding of the thermodynamic role of oxygen interaction within CLS to fully displace all oxygen during sulfidation which enables the fabrication of ceramics with high optical performance. There has yet to be a comprehensive report that outlines all the possible oxygen-related interactions to create a consensus on the role of oxygen in CLS which is necessary to improve upon the current state of the art synthesis and ceramic fabrication techniques.

Table 2 Review of current experimental techniques and challenges faced during the synthesis of CLS powders and subsequent consolidation into polycrystalline ceramics.

	Synthesis			Ceramic Fabrication	
References	Precursor materials	Technique	Results	Processing Route	Results
Beswick [8]	Metal nitrates	Evaporative decomposition of solution (EDS)	Soft, fine powder 0.2 – 2 μm particle size	Hot pressing + HIP, H2S annealing	Max transmission of 60%, absorptions in IR
Tsay [24]	Metal alkoxides	Flowing CS_2 or H_2S in graphite crucible	Mixture of phases at lower temperature, pure γ- phase at 850°C	Pressure-less sintering under H_2S +HIP	Max transmission of 60 %, significant IR absorptions
Durand [16]	Metal nitrates	Combustion, 2-step H_2S sulfidation at 1000 °C and 1250 °C in alumina / silica crucibles	Pure γ- phase $CaLa_2S_4$ power, with 0.025 wt % O	Pressure-less sintering with flowing H_2S / H_2 followed by HIP	Max transmission of 68 % at 12 μm, significant absorptions in 8 – 12 μm region

Problem and Hypothesis

Current understanding of CLS attributes several issues in the powder synthesis and subsequent ceramic densification process to the presence of oxygen. Reports suggest that oxygen may manifest itself as a secondary phase, which subsequently causes both scattering and absorption in the spectral region of interest, or that a single phase of $\gamma - CLS$ may be produced but will be contaminated by impurity groups such as $SO_3^{-2}, SO_4^{-2}, or\ CO_3^{-2}$ as a result of oxygen presence. Such impurity assignments, investigated in the present effort here, have led to the questioning of these attributions. To further enhance the performance of CLS as an infrared optical material, it is imperative to have knowledge of the exact form of O – related impurities that formulate an understanding of the formation mechanism that leads to the problems faced, so that solutions can be defined. It is for this reason that the work presented in this thesis will show that a pure $\gamma - CLS$ phase exists which contains measurable dissolved oxygen present as a substitutional defect within the crystal structure. Both a qualitative and quantitative description of oxygen's presence will be given.

Thesis Overview

In Chapter 2, details of the characterization techniques and protocols being utilized in this project will be presented. This includes the various spectroscopic techniques (IR, and x-ray) and diffraction techniques (x-ray and electron) were performed on the materials under investigation. Chapter 3 then outlines the experimental methods used to prepare samples for their various characterization including the method for determining lattice parameter, measuring samples by spectroscopy, and ceramic densification technique. Chapter 4 then presents and interprets the results obtained on these materials to demonstrate that oxygen exists as a substitutional defect in the CLS crystal structure and present evidence for the other types of O-related impurities that are present. Chapter 5 then outlines the conclusions drawn from this study and proposes remaining questions, ideas, and experiments for future work.

CHAPTER TWO: CHARACTERIZATION TECHNIQUES AND MEASUREMENT PROTOCOLS

Metrology Tools

This chapter summarizes the key tools, techniques and measurement protocols used in carrying out the analysis of powders and ceramics in this thesis. Where noted, specific efforts to ensure no moisture or oxygen contamination could be imparted to the specimen (in powder, powder compact, or ceramic form) during the measurement, are described. Further, this is expanded on in discussions in chapter 3.

X-ray Diffraction (XRD) was used to quantify the lattice parameter of the cubic La_2S_3 crystal structure. Unless otherwise stated, all XRD data for both powders and ceramics was performed at the Materials Characterization Facility (MCF) at UCF on a PANalytical Empyrean diffractometer. An internal standard (LaB_6) powder was used on all samples to correct for any systematic errors during the data collection. A Cu anode was operated at 45 kV and 40 A to generate $K_{\alpha 1}$ and $K_{\alpha 2}$ x-rays with wavelengths of 1.541 and 1.544Å respectively. No additional optics were used to negate the contribution of $K_{\alpha 2}$. Scans were performed from $2\theta = 20° - 70°$ with a step size of $0.0042°$ and integration time of 100 sec/step.

Combustion Analysis - was performed on a LECO ONH 836 elemental analyzer to determine the oxygen content [25]. Samples were placed inside a graphite crucible, then inserted into the reaction chamber. The furnace power was ramped to 3700 W in 39s to completely combust the sample. Using Ar as a carrier gas, the reactants were transported into the CO / CO_2 NIR detectors which analyzed the gas for an integration time of 40 sec.

Fourier Transform Infrared Spectroscopy (FT-IR) was used to characterize the optical transparency of the CLS ceramics. A Nicolet is5 spectrometer was used, collecting data on a singular location on the sample with a 6 mm spot size, and a spectral resolution of 4 cm^{-1}. An average of 32 scans were average in the

spectral range from 7000 cm^{-1} to 500 cm^{-1}. Samples were ground and polished prior to analysis using a Buhler EcoMet grinder polisher with the protocol that is described in chapter 3.

Raman spectroscopy was used to probe the vibrational states related to oxygen. A Horiba LabRAM HR Evolution Nano integrated confocal Raman spectrometer was used operating with an excitation laser at 785 nm was used at 25 % laser power for 10 sec of integration time and 10 accumulations for ceramics and 1 % laser powder with 10 sec integration time over 10 accumulations for powders [26]. Data was collected over a spectral range from 50 – 500 cm^{-1} using a 300 grating. Ceramic samples were ground and polished using the protocol described in chapter 3.

Transmission Electron Microscopy (TEM) was used to observe the crystal structure of CLS and precisely locate oxygen. Samples were prepared using an in-situ lift out method using a FEI Helios Nanolab 600i dual focused ion beam scanning electron microscope to extract and prepare lamellas for the S/TEM analysis. Specimen were coated with ~50 nm of Cr using electron beam evaporation to protect the CLS samples. A FEI® Thermis Z scanning / transmission electron microscope (S/TEM) with Cs probe correction was used to analyze the CLS ceramics. The operating voltage was 200 kV, and the system was equipped with a monochromator, a bottom-mounted FEI Ceta 16M CMOS camera, a Fishione Instruments Model 3000 high angle annular dark- field (HAADF) STEM detector, and a SuperX windowless SDD energy dispersive spectroscopy (EDS) system, with a solid angle of collection of 0.67 sr. Conventional high-resolution (HR-TEM) imaging, HAADF-STEM imaging, and STEM-EDS mapping were performed; for HAADF-STEM work, the probe semi-angle of convergence was 22 mrad and the probe current was set to ~20 pA for high-resolution imaging and ~400 pA for STEM-EDS mapping; the inner collection angle of the HAADF detector for HAADF-STEM imaging was ~70 mrad.

X-ray Photoelectron Spectroscopy (XPS) was utilized to investigate the different bonding environments present in CLS. All XPS measurements were made on a Thermo Fisher Scientific ESCALAB 250 Xi [27]. The ceramic samples were cleaned using a combination of hexane and isopropanol by the protocol explained in [28]. Before data was collected, the surfaces were sputtered using an Ar plasma operating at

500 eV for 600 seconds. Spectra were collected at 300K and 5 x 10^{-8} Pa using an Al Ka monochromatic source. Powder samples were collected using identical conditions. Loose powders were loaded into wells of a custom-built sample holder. No cleaning procedure was used prior to loading into the XPS chamber but were sputtered with the same protocol as the ceramics. A detailed experimental procedure for these measurements can be found in [28-30].

These tools were used with the goal of describing the key crystal structure characteristics of the purchased starting powders and their fabricated polycrystalline ceramics that have a known oxygen contamination. The details of these experimental investigations are summarized in Chapter 3.

CHAPTER THREE: EXPERIMENTAL METHODS

Powder handling protocol for CLS

Lanthanum-rich calcium lanthanum sulfide (molar ratio 90 La_2S_3 :10 CaS) powders under investigation were purchased from separate vendors to eliminate biases from the unique, proprietary powder synthesis used to prepare the 90:10 compound. Figure 2 below provides a flow chart that illustrates the powder handling and fabrication steps used to prepare the CLS ceramics in this study. The image in A) shows the

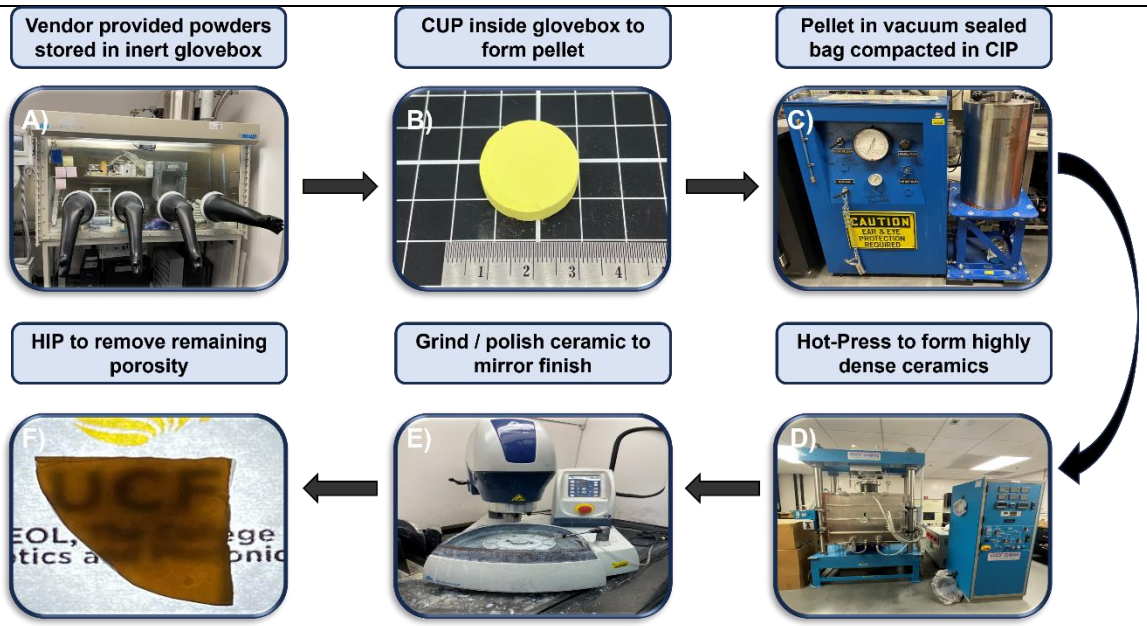

Figure 2 Flow chart summarizing the ceramic fabrication processed used to prepare CLS ceramics via HP and HIP'ing.

glovebox that was used to prevent their interaction with the ambient atmosphere (potential oxidation and/or moisture pickup). The CLS powders were stored in glass jars kept within a MBraun glovebox that operated with ultra-high purity (UHP) N_2 gas. Conditions inside the glovebox were carefully maintained such that O_2 and H_2O concentrations were below 0.1 ppm each. Preparation of the green bodies was initiated inside the same glovebox to further eliminate any potential interaction with O or moisture. The picture in B) shows what a typical CLS green body looked like. To prepare these, ~7 g of CLS powder was added into a 1-inch

stainless steel vacuum die, which was tapped to increase the homogeneity of the particle packing. This die was then connected to a peristaltic vacuum pump to aid the initial compaction of the powders, and was then cold uniaxially pressed (CUP), stepwise, until 3 tons of force was applied. Pressure was held at this maximum load for 2 minutes before pressure was slowly released. The resulting powder compacts were then carefully removed from the die and vacuum sealed in a bag to be removed from the glovebox. The compaction die was cleaned between each use using lint free opto-wipes while inside the glovebox. While the powder compact was still inside the vacuum bag, it was submerged into a liquid bath within a cold isostatic press (CIP) shown in C) where it was further compacted by raising the isostatic pressure to 40 ksi and held at this maximum for 2 minutes before the pressure was slowly released. This was done to increase the relative density of the green body to ~50 % and to reduce its fragility for subsequent handling. Green bodies were subsequently stored within the glovebox until they were hot pressed.

Ceramic fabrication via hot pressing (HP'ing) and hot isostatic pressing (HIP'ing)

Green bodies were removed from the glovebox and loaded into the 1-inch TZM hot press (HP) die in a fume hood. Calcined boron nitride (BN_6) coated graphite spacers were placed around the top, bottom, and circumference of the green bodies to aid in de-molding after sintering. The die assembly was placed inside a custom built OxyGon hot press as seen in D) of figure 2 [31]. The hot press chamber atmosphere was evacuated using a diffusion pump to reach a vacuum pressure of 10^{-6} torr and back filled to 760 torr with gettered UHP N_2 to ensure very high atmospheric purity (no oxygen available for diffusion into sample) during the high temperature HP sintering.

After samples were demolded from the TZM die, ceramic samples were ground and polished on a Buhler EcoMet polishing machine shown in E) of figure 2. Grinding was done on 300 grit and 600 grit SiC paper, and polishing was done on 800 grit, 1200 grit SiC paper, and a microcloth pad that had an alumina polishing slurry (particle size 0.05μm) dispersed across its surface. Polished ceramics had a mirror finish but were examined using a ZYGO white light interferometer to evaluate the surface quality. Resulting ceramics that came out of the HP had high relative densities (4.8 g / cm^3), as measured using the Archimedes method. A

hot isostatic press (HIP) was then utilized at 30 ksi with temperatures ranging between 800 °C – 1200 °C for times between 1 and 10 hrs to finish the densification process. The image in F) of figure 2 shows what a CLS ceramic appears as after it has gone through all these fabrication steps. Surface quality was characterized using a ZYGO white light interferometer (WLI). Polished ceramic samples were assessed using WLI by measuring 5 spots across the top and bottom surface using 10x magnification to obtain representative information of the surface quality. The peak-to-valley (PV) ratio and root mean square (RMS) values were used as the key metrics in determining surface finish as described above. The PV ratio provides a quantification of the total deviation from planarity for a sample, and RMS provides information regarding the overall homogeneity of the surface finish. Typical PV values were 1.2 μm and a RMS of 0.060 μm was obtained for ceramics used for all optical measurements.

Crystal structure characterization

Quantification of the total oxygen percentage for samples was done using the combustion analysis previously outlined in chapter 2. Both powder and ceramic samples were investigated. Verification of the La:Ca ratio is significant to the densification of the powder and resulting optical properties of the ceramics because CLS exists as a complete solid solution between $CaLa_2S_4$ and pure La_2S_3. This target (molar) ratio for a 90:10 composition should be 18 as compared to a ratio of 2 for a stoichiometric 50:50 composition. It has been reported that the lattice parameter increases as the La concentration increases towards the La_2S_3 end member of the solid solution due to the size difference between La^{3+} and Ca^{2+} [11] Measurement of the lattice parameter via X-ray diffraction (XRD) provides insight into this ratio. This ratio could be further altered by changes in cation to anion ratio, or by oxygen substitution of sulfur, a premise of our hypothesis in this study. Lattice parameters of powders and ceramics were determined by computing the value of a for each diffraction peak obtained from a XRD spectrum using the equation:

$$a = d\sqrt{h^2 + k^2 + l^2} \quad (1)$$

where d is the interatomic spacing of a given crystallographic plane denoted by its Miller indices h, k, and l. Calculated lattice parameters were then plotted against the extrapolation function [32]

$$\frac{Cos^2(\theta)}{Sin(\theta)} \quad (2)$$

Here, theta (θ) is the position of the diffraction peak (recorded as 2 θ). By plotting the results from equation (2) versus (1) and performing a linear regression to determine the y- intercept value, one obtains the value of a the lattice parameter for the measured powder or ceramic. This method allows for accurate lattice parameter determination (+/- 0.001Å), despite the apparent misalignment from the plane of diffraction of any given sample within the diffractometer [32]. This effect arises from sample preparation that creates a deviation from planarity when mounting a given sample onto the diffractometer, resulting in one region of the sample to be raised (or lowered) with respect to the instrument's calibrated diffraction plane, resulting in an error in the observed value of 2 θ. This will cause a systematic decrease in lattice parameter as the value of θ decreases. Equation (2) provides a correction factor to the values of a that are calculated from these 2θ values and allows for an extrapolation to be accurately done to determine the true lattice parameter. For samples that were misaligned, a linear relationship exists between the values calculated from (1) and (2). Misalignment was particularly pronounced for ceramic samples, but not powder samples. Figure 3 shows an example of the calculated lattice parameters for 90:10 powders and ceramics procured from vendor 2, which illustrates the significant misalignment of the ceramic samples. This is concluded to be due to the linear relationship between equations. 1 and 2, and high R^2 value. Powder samples did not present issues faced with misalignment, however. Misalignment issues are not typically found using modern XRD instrumentation that have adequate sample mounts and Z-alignment capabilities. The error associated with XRD is important to this calculation of the lattice parameter and was quantified by calculating the standard deviation of the lattice parameter of an internal standard, LaB_6. This internal standard was present for each measurement as it was integrated into the sample (either the powder mixture or onto a ceramic) to serve as a baseline reference. For ceramics prepared via figure 2 with no further processing confirmation of the phase assignment and purity were investigated using TEM. Very thin lamellas were prepared by first

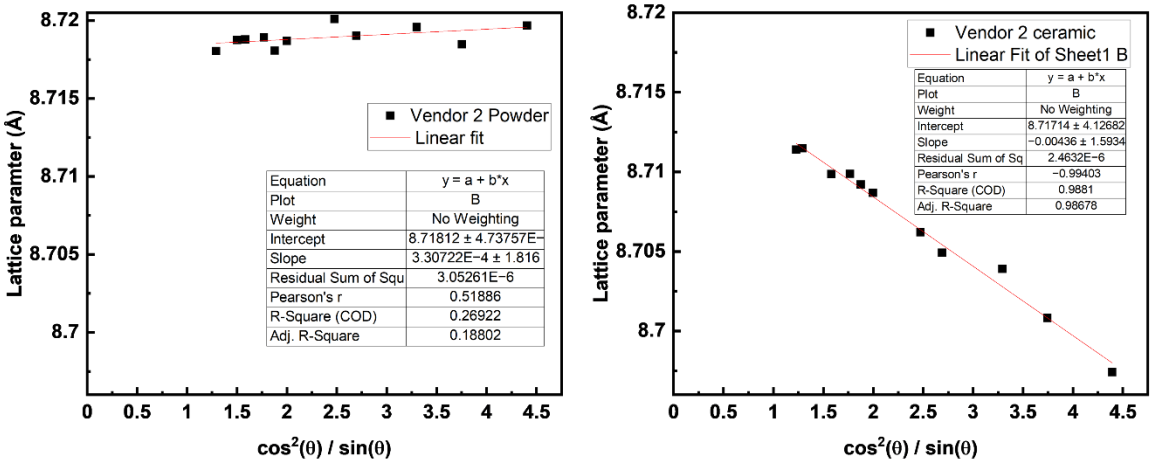

Figure 3 Example of extrapolation method used to determine the lattice parameter, a, on ceramics fabricated (right); lattice parameter for the powder from vendor 2 (left) is shown for comparison.

grinding samples down to 5 μm then, further thinned and extracted using a focused ion-beam (FIB) lift-out technique. A thin protective layer of Pt was deposited on the surface where the desired sample was to be taken from.

Measuring oxygen using IR, Raman, and X-ray photoelectron spectroscopy

Understanding the IR light – matter interactions is of high importance for CLS due to its transparency window being in the MIR - LWIR spectral region. This attribute, broadband IR transmission, is one of the primary desirable attributes of CLS ceramics and it is well documented that oxygen in CLS introduces undesirable absorption in key IR bands. Further, IR spectroscopic techniques provide vital information about the material's (or impurity's) vibrational energies. This aids in the identification of bonding environments associated with oxygen (or other impurities) because CLS is theoretically transparent in the 5 to 16 μm spectral region [8]. In the present study, FT-IR transmission measurements were collected using samples prepared as described in chapter 2. Loss associated with scattering (surface and bulk contributions) and loss (from impurity absorption and Fresnel loss) are integrated into a FT-IR spectrum of a polished

coupon. This data provides information on sample uniformity (within coupon compositional and microstructural uniformity) and the resulting attributes of coupons prepared with varying processing conditions. Raman spectroscopy was also utilized to narrow down and corroborate the possible bonding configurations that could be present for metal-oxygen bonding in the CLS crystal structure. As described above, optically polished ceramic samples were measured using a Horiba LabRAM Raman system to collect this data. The same ceramics were further prepared for measurement in the XPS instrument by fracturing a small piece of the polished sample to measure the cross section to investigate the bulk of the sample and minimize the surface biases that may arise due to polishing. The data acquisition parameters are detailed above in chapter 2.

CHAPTER FOUR: RESULTS AND DISCUSSION

Phase Purity Determination of La-Rich CLS

To quantify the total oxygen concentration in the purchased CLS powders and fabricated ceramics, a combustion analysis was performed by the LECO corporation. Materials were heated to temperatures over 2000 °C in a graphite crucible to completely combust the sample. The gas produced was then measured using IR spectroscopy at fixed wavelengths corresponding to CO/CO_2 absorptions. The resulting data can be seen in table 3 below. Oxygen content remains relatively equal between the powder purchased from vendor 1 and 2. O also remained approximately constant from the vendor 2 powders to ceramics, suggesting that the powder synthesis was likely the source of oxygen in the materials, and was therefore not picked up during the power handling and ceramic processing. Comparing this data to the previous quantification done by Durand shows that these powders have nearly double the oxygen content, as compared to the powders that he studied [16]. This finding is interesting when next considering the XRD patterns below. Figure 4 shows the XRD patterns for the powders purchased from the two vendors. Although both materials have similar O concentrations, their XRD patterns show clear differences, in that the powder from vendor 2 shows signatures for the β-phase, evident when zooming in on a key region of 2θ between 30 – 40 °. Vendor 1 powders however show a phase pure, cubic system. To determine the effect on phase purity after sintering these powders, XRD was collected again polished surface using the protocol outlined in chapter 2. Figure 5 below shows the patterns

Table 3 Quantification of oxygen in CLS powders and ceramics.

Sample	O wt%
Vendor 1 powder	0.0550
Vendor 2 powder	0.0554
Vendor 2 ceramic	0.0515

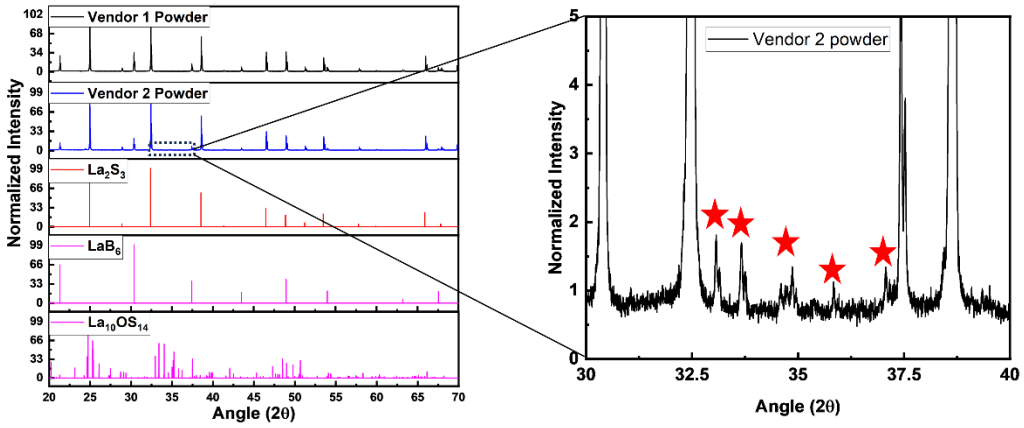

Figure 4 XRD of vendor 1 and 2 powders (left) and a zoom in on the region of interest showing the β-phase ($La_{10}OS_{14}$) present for the vendor 2 powder. The red stars indicate peaks associated to the β-phase La_2S_3, $La_{10}OS_{14}$ and an internal standard LaB_6 are shown below the experimental data for reference.

of these ceramics. What is evident again is that the ceramic prepared from vendor 2 powder shows a signature for the β- phase, although the peaks associated to this phase do not appear to have increased in their intensity, suggesting their concentration remains equivalent. Comparison of these patterns to an experimental XRD pattern of Ca free γ-La_2S_3 shows that both the 90:10 powders and ceramics had the same cubic symmetry. Adherence to the selection rule $h + k + l = 4n$ confirms the space group of $I\bar{4}3d$, which categorize the Th_3P_4 type crystal structure [4]. There is a slight decrease in lattice parameter that is observed as shown in Table 2 with lattice parameter values from Mauricot and from Luguev *et al*., provided for comparison. As excepted, the lattice parameter for the 90:10 CLS powders and ceramics are smaller than that of La_2S_3. When compared to the value determined by Luguev for the same stoichiometric ratio of La:Ca, there is a slight decrease in the lattice parameter. If the materials presented in this work contain more oxygen dissolved throughout the structure, then it is likely that the lattice would cause a shrinkage effects due to its difference in radii compared to S [33]. However, the error associated with the lattice parameter calculation is greater than the difference between the reference from Luguev and the data presented here. Using LaB_6

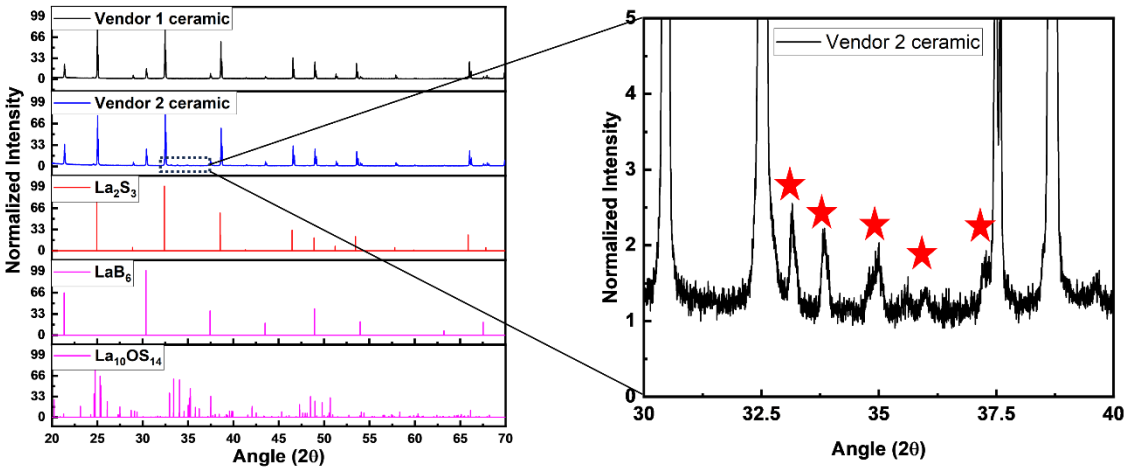

Figure 5 XRD of prepared ceramics from vendor 1 and 2 powders (left). Zoom in on the small region of interest showing the β-phase ($La_{10}OS_{14}$) present for the vendor 2 ceramic. The red stars indicate peaks associated to the β-phase. La_2S_3, $La_{10}OS_{14}$ and an internal standard LaB_6 are shown below the experimental data for reference.

Table 4 Lattice parameters of vendor 1 and 2 powders and the ceramics fabricated by HP + HIP procedure.

	La_2S_3 [34]	La_2S_3 [11]	Vendor 1 lot 2	Vendor 2 lot 2
Powder	8.723 Å	8.721 Å	8.718 ± 7.77 x 10^{-4}Å	8.718 ± 7.77 x 10^{-4}Å
Ceramic	-	-	8.719 ± 7.77 x 10^{-4}Å	8.717 ± 7.77 x 10^{-4}Å

as an internal standard confirms that the lattice parameter calculations determined from these XRD data are accurate to 7.7 x 10^{-4}Å. The lattice parameter, within the error of the measurement, for each ceramic after HP appears to be unaltered as compared to their parent powders, for both vendors. It is interesting to note that the presence of low levels of O only minorly changes the lattice size and doesn't necessarily affect the cubic nature of CLS. Although the vendor 2 material shows signs of secondary phase that could be associated to O, the vendor 1 powder and ceramic show no incorporation of any secondary phase and a similar concentration of O present. This observation, that O and S may co-exist in a phase pure crystal

structure was first made on an analogous isostructural system, γ-Ce_2S_3 by Eastman [35]. He noted that at various O to S ratios, the crystal structure could take on either that of the oxide (at high O), the sulfide (at low O) or a distinct structure from either the oxide or sulfide (intermediate O). The XRD data here supports this idea but does not provide insight into how the O may be incorporated into the CLS structure. Therefore, the commonly employed XRD characterization technique does not provide a simple method to determine the presence of O. Further, as XRD also has a limitation in the sensitivity to ~1 vol%, TEM techniques were utilized to confirm the phase purity of the vendor 1 ceramic material.

In search of any secondary phases (especially the β- phase) a 10 x 10 μm cross section of the vendor 1 ceramic was investigated, through its bulk and in its grain boundaries. HAADF images with their respective SAED patterns of two individual grains from the vendor 1 ceramic are presented in figure 6. The top micrograph shows the cross section of the ceramic where four distinct, identifiable grains can be observed. SAED data was collected on each of these individually, this data can be found in the appendix for the

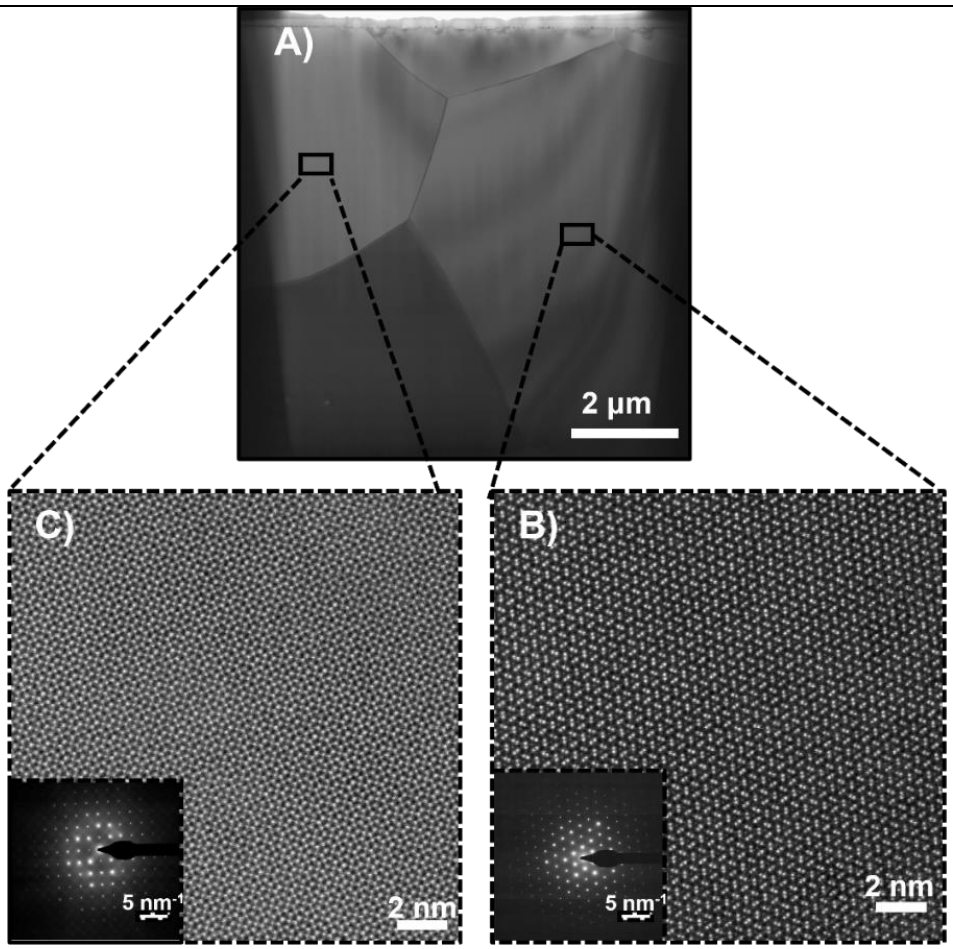

Figure 6 A) Cross section of lamella showing four distinct grains. B) HAADF image of the top grain with SAED inlayed showing zone axis to be [111]. C) HAADF image of bottom grain with SAED inlayed showing zone axis to be [100].

remaining two grains. Figures B and C show the HAADF images captured viewed down the (111) and (100) planes respectively. Throughout these micrographs for both the grains presented here, there is no observable breakage in the expected symmetry or point defects that could be associated to O. Scanning transmission electron microscopy coupled energy dispersive x-ray spectroscopy (STEM-EDS) data was also collected on the same CLS ceramic prepared from vendor 1 shown in figure 7. The top left side of the figure 7 presents a rendering of the CLS structure as viewed down the (111) direction. The top right map in figure 7 shows the overlayed positions of La (red) and S (green) atoms down the plane (111). The

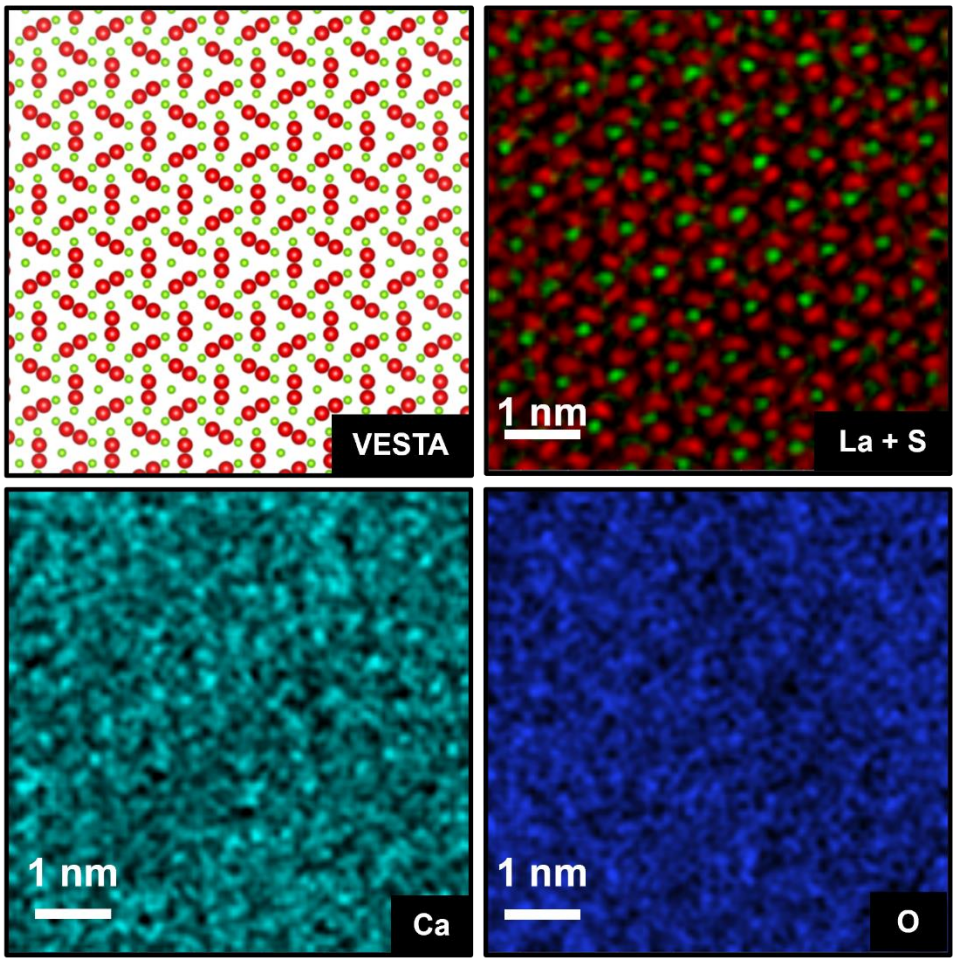

Figure 7 Model of Th_3P_4 structure of La_2S_3 looking down plane (111) compared to overlayed EDS compositional maps of La in red and S in green. Ca is shown in grey and the composition map shows weak correlation with La signals. The O signal in blue appears smeared throughout the micrograph.

dumbbell geometry of La atoms in coordination around a central S atom in continuous repetition is characteristic of the Th_3P_4 crystal structure and strongly resembles the HAADF images. The apparent lack of vacancies within the crystal structure in both the HAADF and EDS could be due to the randomness of the vacancy formation which will 'hide' the appearance of vacancies. Strong La signals that would likely appear from behind where the vacancy would be located at could create an illusion of a vacancy-free structure. Alternatively, observing little to no vacancies may be indicative of a departure from the desired $La{:}S$ of 1.5. The Ca signal that is shown appears to be weak and blurred, however due to the small

concentration of Ca present in this sample, this is to be expected. The signal for Ca appears to be weakly correlated to the La signal as it should due to Ca residing on equivalent 12a sites. The presence of oxygen was also apparent while collecting the EDS data. This signal appeared weak and 'smeared' throughout the sample and thus did not provide insight into its location within the crystalline structure but reinforces its presence. However, both the HAADF and EDS data suggest that there are no secondary phases within the bulk of the CLS grains for the ceramic prepared from vendor 1 powder. To verify that secondary phases also do not appear in regions of high disorder, images were also collected at the grain boundaries. Figure 8 shows HAADF images of a triple junction (left) of three CLS grains adjacent to each other. On the right is a zoomed in image that shows the very clean, thin grain boundary that exists between these two crystallites. This supports the notion that there is not a presence of secondary phase in this material. It is of significantly high importance to have thin grain boundaries that are free from secondary phases to reduce the total scattering of the material and maximize its transmission. Combination of SAED, STEM-EDX with XRD data strongly suggests that the materials used in this study exhibited the optically desired γ-phase but do not elucidate the structural role of oxygen. Additionally, TEM analysis shows that O is uniformly integrated throughout the lattice network with no spatial preference to a specific location. However, to complete this interpretation with more environment specific information that TEM mapping cannot provide, we turn to IR spectroscopic techniques aimed to associate vibrational modes with different bond types in the CLS ceramics.

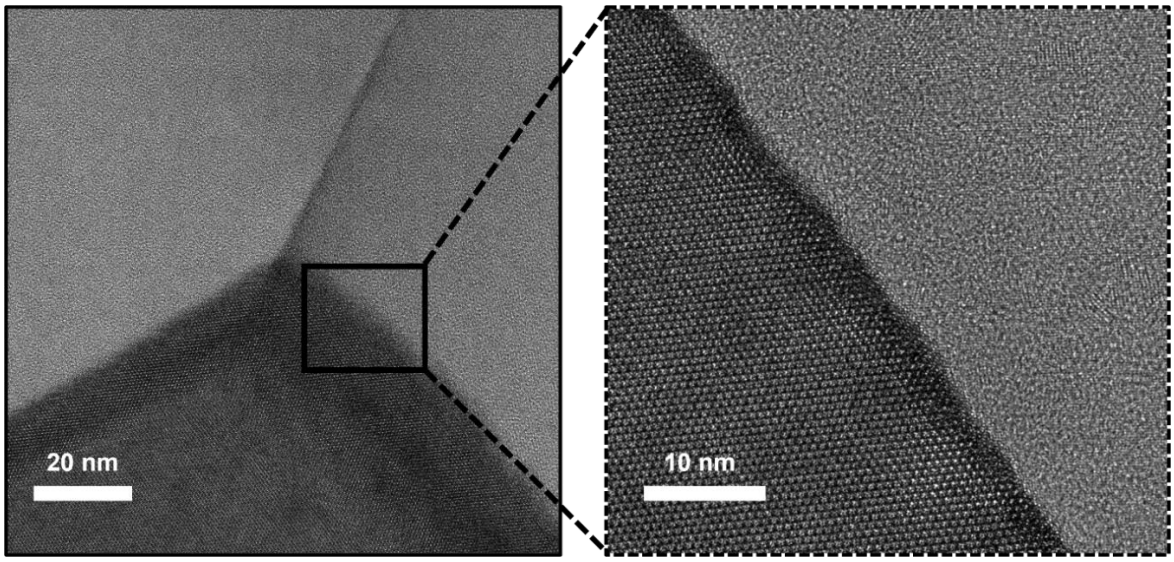

Figure 8 Left: zoomed out HAADF micrograph of triple junction captured on vendor 1 ceramic Right: zoomed in HAADF of grain boundary between rightmost grains showing clean interface between two grains and no 2nd phases detected at grain boundaries.

Infrared optical properties and role of oxygen in CLS structure

Prepared (HP+HIP'd) CLS ceramics were measured using in-line FT-IR transmission to investigate their optical properties. Shown in figure 9 (left) is an FT-IR transmission spectrum of two CLS ceramics of thickness t = 2.22 mm for vendor 2 and 1.96 mm for vendor 1. Shown for comparison (right) are data from other researchers on stoichiometric $CaLa_2S_4$ compositions rather than the UCF 90:10 composition. Figure 9 (left) shows the significant difference that can be observed in the optical transparency of the two ceramic materials prepared under identical processing conditions. Here, one can see that the ceramic prepared from vendor 2 powder has a nearly 30 % increase in transmission at 10 μm. Although there is not a significant difference in the band gap which would indicate a substantial stoichiometric shift in the number of vacancies toward the La_3S_4-like structure – an electrically conductive material with large free carrier absorption, we suggest a few alternative mechanisms that could potentially account for this difference. Firstly, the variation could be associated with a variation in free carrier absorption. It has been shown in the analogous Ce_2S_3 –

Ce_3S_4 system that as the number of structural cation vacancies is decreased, the number of free carriers are significantly increased because bond formation between Ce^{3+} and S^{2-} occurs such that an extra electron becomes delocalized among the large Ce atoms and can be described by a small polaron band model [36]. Indeed, a shift in the band gap will become apparent if a significant amount of this structural rearrangement has occurred. However, if this effect is less pronounced, a polaron may only appear as distinct sub-band gap absorptions that appear as equally spaced absorptions that decrease in magnitude as a function of energy. Regardless, for CLS materials to achieve their maximum transmission, it is imperative for their cation:anion ratio to be tightly controlled. This means that depending on the chosen composition there are necessary structural cation vacancies that must be preserved, except in the case of stoichiometric $CaLa_2S_4$

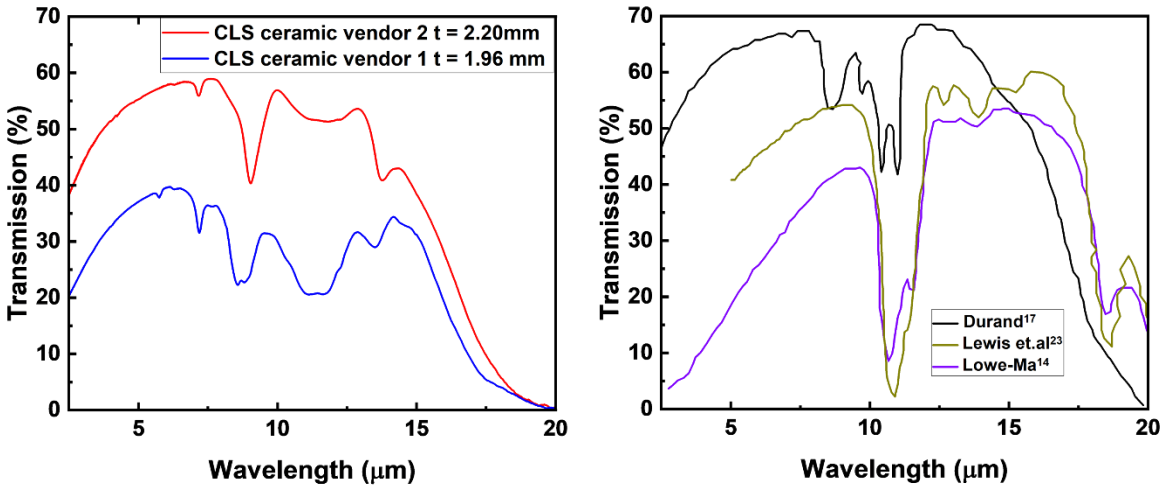

Figure 9 Left: FT-IR transmission spectra of ceramics prepared from powders purchased from vendor 1 (blue) and vendor 2 (red). Right: FT-IR spectra from various literature sources highlighting the myriad of absorption peaks that have been reported for CLS ceramic.

(50:50 composition) where all vacant sites are occupied by Ca^{2+} [37]. In addition to the conclusions that can be drawn regarding the stoichiometry of the materials, the FT-IR data shown in the UCF data depicted for ceramics from vendors 1 and 2 on the left side of figure 9 also reveals several absorption bands of varying broadness can be seen in the 5 to 15 μm spectra region, which provide information regarding the

impurities present. These bands, at 5.74 μm, 6.28 μm, 7.18 μm, 7.61μm, 8.57 μm, 8.82 μm, 9.04 μm, 10.31 11.04 μm, 11.70 μm, 12.24, 13.57 μm,14.48 μm, and 17.4 μm have been ascribed in prior studies to various species. Literature provides explanations for some of the various absorptions observed in this region. The right side of figure 9 compares the transmission spectra for various references. Though there is some overlap with regards to peak position of specific absorptions (absorption at ~11 μm for example) the relative intensities, total number of peaks, and their relative positions vary [14, 16, 38]. Regardless of these differences, assignments of peaks have been consistently attributed to groups of SO_3^{-2} and or SO_4^{-2} [15]. Other than circumstantial evidence of SO_4^{-2} and SO_3^{-2} having strong resonances at similar energies, there is no basis to the argument of the presence of such groups. We can make this claim by considering first that the point group for a free SO_4^{-2} ion is T_d and when constrained within a crystal, its symmetry may be lowered to either C_{2v} or C_{3v} depending on how the oxygen present coordinates to its surrounding metal atoms. Therefore, for an SO_4^{-2} group to be present, there must be tetrahedrally coordinated O surrounding a S atom that is further bound to its nearest metal cation. For a SO_3^{-2} group, there must be pyramidal symmetry about the S atom, in which either the S atom or O atom can coordinate with a neighboring metal atom yielding either C_{3v} or C_s point group respectively. Table 5 below provides a summary for the point group analysis done on these impurity groups, showing the maximum number of IR active modes one might expect from such coordinated species in our CLS. Experimental evidence does indeed support the notion that these groups may be present, though these species were not found by a complementary analysis. The number of active modes that appear for any one impurity group does not correlate to the number of absorptions that are observed in figure 9. It requires that there be a combination of sulfato complexes present in the material. Assertion of such impurity groups causes one to reconcile the necessary redox states that arise due to electron transfer that occurs in these compounds. For either SO_4^{2-} or SO_3^{2-} the two extra electrons are shared between equivalent structures that transfer the two additional electrons between the central S atom, forming an S^{2-} state and the surrounding bonded O atoms, forming an S^{2+} for SO_4^{2-} and S^{3+} for SO_3^{2-} causing an effectively neutral S^0 for both ions. In CLS, a given S is in its -2 valence state, so the

Table 5 IR and Raman active modes for sulfate and sulfite groups with varying symmetries.

Point Group	IR Modes	Total
T_d	$2T_2$	2
C_{3v} (SO_4)	$3A_1 + 3E$	6
C_{2v}	$4A_1 + 2B_1 + 2B_2$	8
C_{3v} (SO_3)	$2A_1 + 2E$	4
C_s	$6A' + 2A''$	8

existence of an SO_4^{2-} or SO_3^{2-} implies that S has mixed valency, between S^0 and S^{2-}. Further, the question that arises from this assignment of sulfate / sulfite groups which could be incorporated into the crystal structure, is how the structure of CLS can maintain cubic symmetry. These types of impurities are unlikely to exist as free ions, they should be found in bonds to either La or Ca. If such impurities were present, then secondary or tertiary phases should be recognized by other characterization methods as there must be a significant disruption to the crystalline lattice to find four oxygens surrounding one sulfur, presumably where oxygen is occupying cation sites. As shown previously in the XRD data, no evidence of these extra phases (such as $La_2(SO_4)_3$ are present. Another scenario that may be thought up is that the S-O bonding is not an interaction between nearest neighbors, but second nearest neighbors. The next nearest S (in relation to a central sulfur atom) may be substituted by oxygen, which creates an asymmetry that pulls itself closer to the central sulfur atom, thus forming a bond that resonates at the observed energies. However, this is very unlikely to occur, considering the typical bond lengths for an S-O bond that produces absorptions at these wavelengths (6-13 μm) is 1.4 Å, while the S-S atomic distance is 3.2 Å [4, 34]. Again, such interactions would create significant distortions to the crystal lattice of CLS and are thus unlikely. An interesting possibility is for O to be present as an interstitial defect because this could more accurately explain the vast differences (in magnitude, position, number of absorptions) observed between the two UCF ceramics shown in figure 9 and the literature data. There are numerous possible bonding environments that can be arranged

with the CLS crystal structure, so an interstitial O would have many possible bonding environments that could give rise to the absorptions in the 5 to 15 μm region with S-O interactions. For the case in which O substitutes a S atom on an anion site, the La-O or Ca-O resonances that would result are not expected to be found at the high frequencies (5 – 15 μm) observed in these materials. However, as will be shown in subsequent sections utilizing XPS and Raman spectroscopy, La-O bonds do present themselves. Additionally, evidence will be presented that supports the XRD and FT-IR analysis that sulfate and sulfite groups are not present.

Despite being a surface sensitive technique, XPS can provide valuable insight as a commonly utilized characterization technique that can distinguish between different bonding environments, hence providing insight into how O is integrated into the CLS network. While IR spectroscopic techniques aimed to associate vibrational modes with different bond types in the CLS ceramics, these methods are not quantitative and require assumptions based on geometry of said bonds, and their bond strengths. A complimentary tool for quantitative determination of bond types is needed. Although XPS is a surface sensitive technique, with proper sample preparation the bonding environments of key atoms can be understood. To support the hypothesis that O substitutes itself into S sites, XPS was used to examine the bonding environments of S and O. Looking at the fine spectra acquired for oxygen and sulfur in figure 10, bonding environments between various constituent elements can be established. Starting with the fine spectra of the 2p orbitals for S, there is a mono-peak centered at ~162 eVs. For 2p orbitals it is expected to observe doublet peaks due to the splitting of the 3/2 and 5/2 spin-coupled orbitals. The appearance of this singular peak indicates that there are multiple bonding environments present for S in this material that causes overlap in the XPS signal. The deconvolution of this peak indicates that there are two distinct environments present. At lower binding energy, there is one environment that is associated to M-S type bonding and at slightly higher binding energy another than is interpreted as a S-rich M-S type bonding. No signature appears however for the presence of impurity groups such as sulfates or sulfites. Distinct peaks or a tertiary shoulder would appear in the 164 to 175 eV region if such impurities existed. Rather, there is

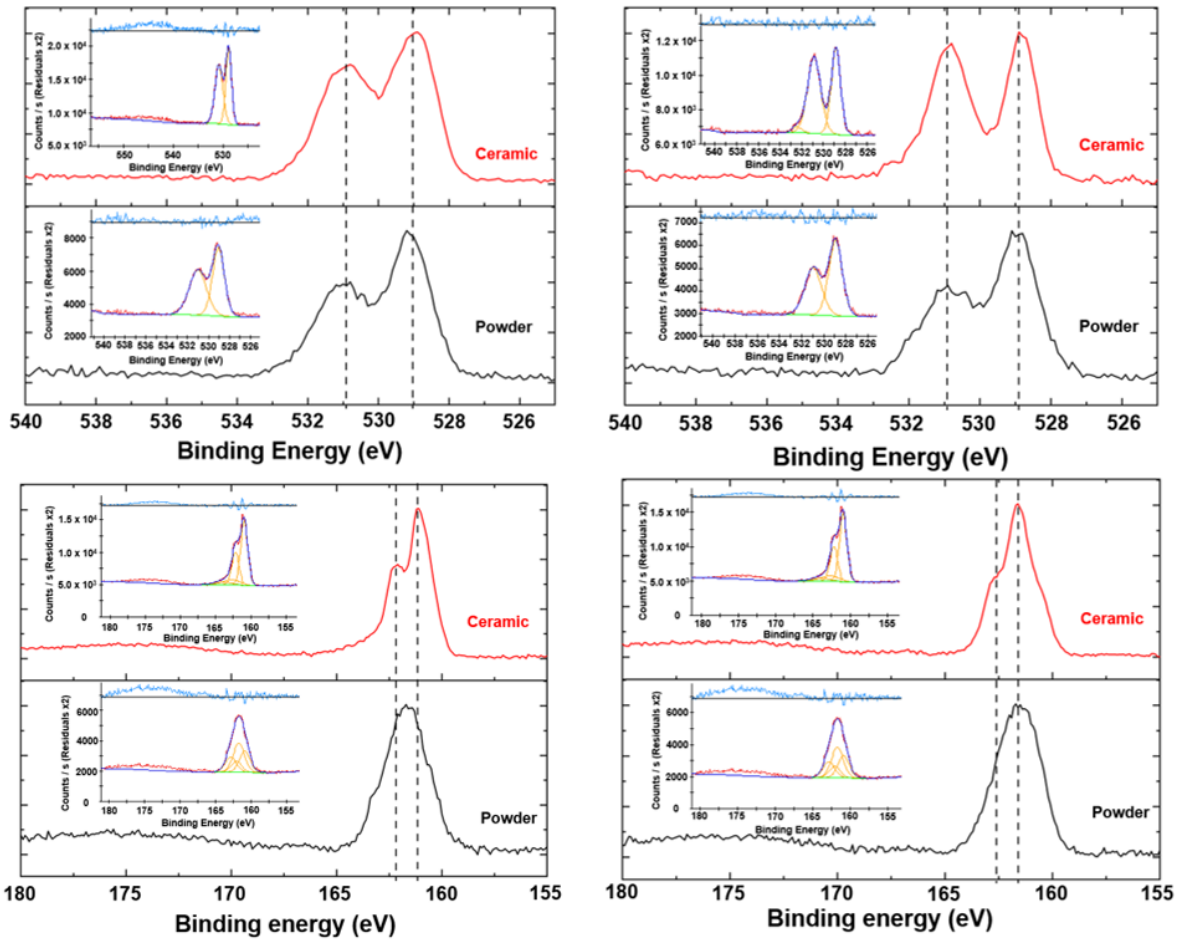

Figure 10 XPS fine spectra of S (top) and O (bottom) collected on powders (black) and ceramics (red) prepared from vendors 1 (left) and vendor 2 (right).

a broad, weak signal that appears in the 170 eV – 180 eV region that is attributable to a plasmon of La [40]. The 2p orbital of S appears in a region that is situated in between the 3p and 3d orbitals of La, and this plasmon is well documented [40]. The fine spectra of the O 1s orbital also indicates multiple bonding environments present. Only 1 peak should appear for a 1s orbital because there is no spin-orbit coupling effect that would cause a splitting into multiple peaks [40]. Deconvolution of these peaks indicates characteristic signature of La-O (529 eV) bonding environment [40]. At higher binding energy (531 eV) the peak is not fully understood currently, though it is hypothesized to be attributed to surface oxidation of

the La-O bonds to form La-OH [40]. respectively. This data corroborates the XRD data regarding the lack of presence of secondary phases associated with Ca or La sulfates or sulfites. Further, this observation and the clear La-O signature supports the hypothesis that O exists as a dissolved impurity in the CLS crystal structure. The reported XPS data thus supports the hypothesis that O substitutes itself into the S sites of the CLS crystal. Considering the possible bonding environments for a substitutional oxygen, its interactions with Ca, or La would lead to distinctive features in vibrational spectra measured by either Raman or FTIR. The large reduced mass of such bonds would push the absorption bands into wavelengths longer than the lowest energy absorption shown in figure 9.

To support this hypothesis of O as a substitutional defect in 90:10 CLS, analysis based on Raman spectroscopy was utilized. If oxygen does substitute sulfur on the anion sublattice, then it would be natural to expect it to be bound to either La or Ca. Due to high reduced masses of these bonds, we would not expect to see local absorptions in the 5 to 15 μm region. Rather, resonances would be more likely found at longer wavelengths [41].

To create a model for the phonon density of states for the 90:10 CLS, a simple diatomic linear chain consisting of alternating La-S bonds was chosen. Cyclic Born-Von Karman boundary conditions are used. The La-S distance is 3.02 Å (average La-S distance in CLS) and a transverse spring constant for the La-S bond of $k_{La\text{-}S}$ = 34 N/m was chosen to set the value of the resonant transverse optical (TO) mode at the Γ point at 210 cm^{-1}. The resulting phonon density of states can be seen in fig. 11 below, which shows the transverse acoustic (TA) branch from 0 – 90 cm^{-1} and the TO branch straddling about 200 cm^{-1}. To model a substitutional O, one sulfur atom was removed from the diatomic chain such that a single La-O-La unit was created in the center of the chain and surrounded by La-S bonds. In doing so, the same TA and TO branches are observed, with the inclusion of two weak local vibrational modes that appear at ~ 100 cm^{-1} and 360 cm^{-1}. Comparing this calculation to the experimental Raman spectroscopy data of a vendor 1 ceramic, in figure 15, shows an agreement in the resonant frequency of a La-O local modes. The weak but

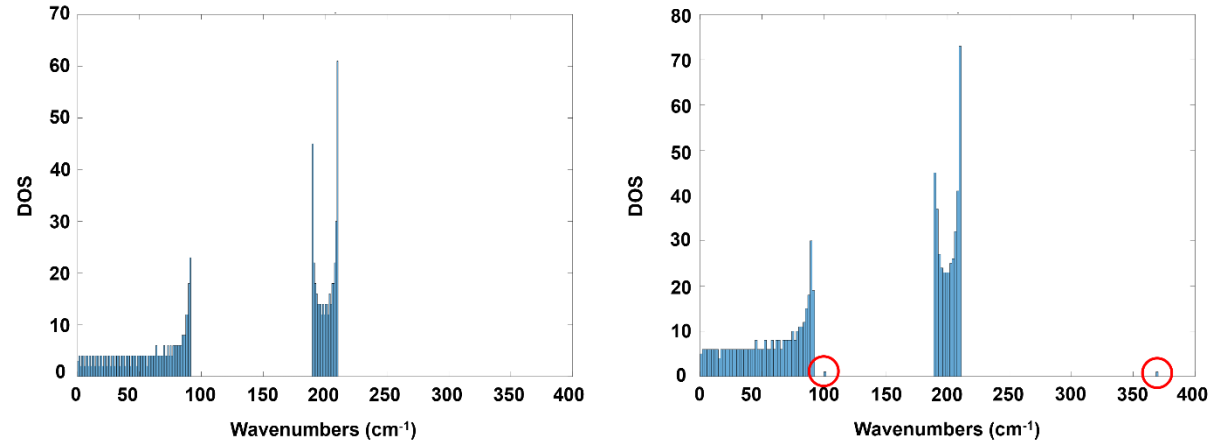

Figure 11 DOS calculation on quasi-infinite 1-D La-S chain without O (left) showing the TA and TO phonon branches associated with CLS. DOS calculation of same linear chain with one O substitutional defect showing local vibrational modes circled in red.

noticeable features at 110 cm^{-1} and 380 cm^{-1} support the prediction made by this simple model. Further, it has been shown by Merzbacher, that the highest frequency phonon mode for CLS should appear at 320 cm^{-1} [42]. The appearance of the mode at 380 cm^{-1} is well beyond this cutoff point and is very likely to be associated with substitutional O. Assignment of the lower frequency mode at 110 cm^{-1} comes with the caveat that not all the phonon modes have been determined yet for CLS. It is possible that this could be

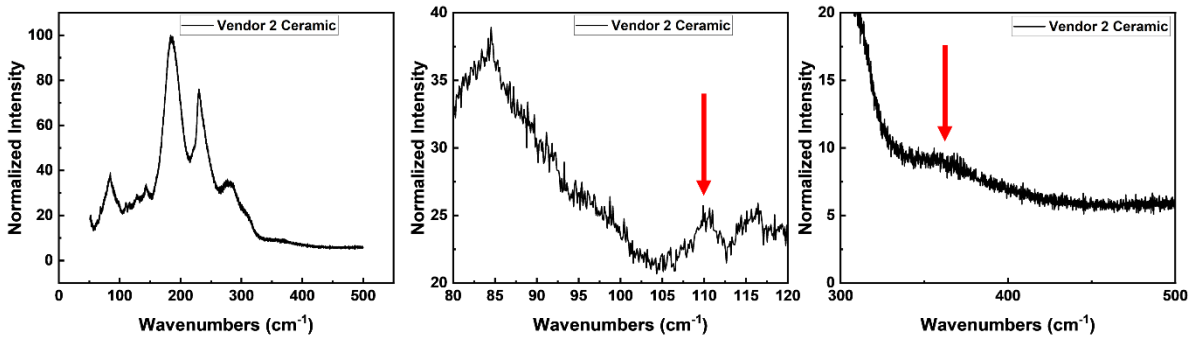

Figure 12 Experimental Raman spectra of the vendor 2 ceramic collected from 50 cm^{-1} to 500 cm^{-1}, and zoomed in on the regions where predicted local vibration modes exist for La-O bonds.

attributable to a fundamental CLS phonon, however it has been suggested that these remaining modes may appear at even lower frequencies, below 50 cm^{-1} and have yet to be observed experimentally. Correlations between the FT-IR and Raman data can be made when comparing the quantifications made by XPS. For both CLS ceramics, the S at % remains approximately equal. O however, is significantly higher for the vendor 1 ceramic than it is for the vendor 2 ceramic. Deconvolution of the two O peaks allows for quantification of both bond types, and it was determined that the La-O remains approximately equal (within the XPS uncertainty of 1 at %) at 2.74 and 3.45 at % for vendor 1 and 2 respectively. This apparent matching of substitutional oxygen, at low concentration, matches the observed intensity in the Raman analysis as both materials show consistent weak modes at the predicted frequencies (see appendix 1 for the Vendor 1 Raman spectra). This may be indicative of the maximum quantity of O that may be substituted onto S sites.

Table 6 XPS quantification of relevant elements present in the vendor 1 and vendor 2 ceramics.

Element Quantification	Vendor 1 CLS Ceramic	Vendor 2 CLS Ceramic
At % S	45.3	46.4
At % O	8.3	6.11
At % Other-O	5.56	2.66
At % O-La	2.74	3.45

The concentration of the other-O however varies from 5.56 at% for vendor 1 to 2.66 at% for vendor 2. The discrepancy of the other-O quantification provides useful information regarding the absorptions in the 5-15 μm spectral region, as it can be asserted that substitutional O is not responsible for these absorptions. Considering that neither the XRD, FT-IR, or XPS analysis provide observations that are consistent with presence of sulfate groups there must be another type of bound O in the CLS system. Two possible scenarios may be devised. First, it is possible that the O signal that is interpreted as Other-O may be a signature of interstitial O. In this case the interstitial may reside closer to the S within the structure and give rise to the complex absorptions observed in the FT-IR spectra. Secondly, it is possible that O has substituted itself into

vacant sites on cation sublattice. It has been previously thought that the it could be possible to have an anion sit onto a cation site in a similar Th_3P_4 type chalcogenide structure [43]. Further, it was shown that O substitution for a La on regular cation sites is energetically favorable, and similar to that of a substitution of O for S [44]. This makes an interesting case for the possibility of O substituted onto cation sites. Elucidating this information is of the highest importance regarding the development of CLS. By distinguishing how O prefers to arrange itself within the crystal lattice will provide useful information regarding future synthesis to displace the different known types of O.

CHAPTER FIVE: CONCLUSIONS

Research presented in this thesis has aimed to understand oxygen's role in the CLS crystal structure by studying hot pressed ceramics and their starting powder materials. Compiling the findings from multiple characterization methods observed for 90:10 CLS powder procured from (2) vendors illustrate the following key results:

1. Oxygen can dissolve into the cubic γ-CLS as a substitutional anion defect, and possibly as an interstitial defect or a substitutional defect onto cation sites,
2. IR and Raman spectroscopy provide simple non-destructive tools to provide crucial information regarding the role of O in CLS,
3. Agreement between XRD / TEM and FT-IR / Raman / XPS techniques provide substantial evidence for substituted O and therefore are useful tools to aid the synthesis of CLS.

From these findings, it is possible to narrow optimal synthesis parameters to create CLS that is not only phase pure, but of very low impurity content. The question of concretely identifying the local modes that are responsible for the IR absorption features remains. To understand this, utilizing HRTEM will be invaluable to capture the location of oxygen in relation to the CLS crystal structure. Furthermore, acquiring IR and Raman spectroscopy data from NIR – LWIR will provide the necessary constraints to determine the form of oxygen by providing information on its local symmetry. It is still unclear how the incorporation of oxygen affects the lattice parameter of CLS. This likely will require modelling efforts to deconvolute the varying effects from S loss, La content, along with O content. To monitor O in powders, Raman and IR diffuse reflectance spectroscopies can be utilized. To understand the role of stoichiometry, which effects the maximum transmission, a full thermoelectric characterization study of these materials will provide one with a great majority of the required knowledge on the defect chemistry of this material, particularly related to the cation to anion ratio. The observations and analysis shown here provide a step closer to understanding the current pitfalls in fabricating CLS ceramics with optimal IR performance.

APPENDIX: SUPPLEMENTAL DATA

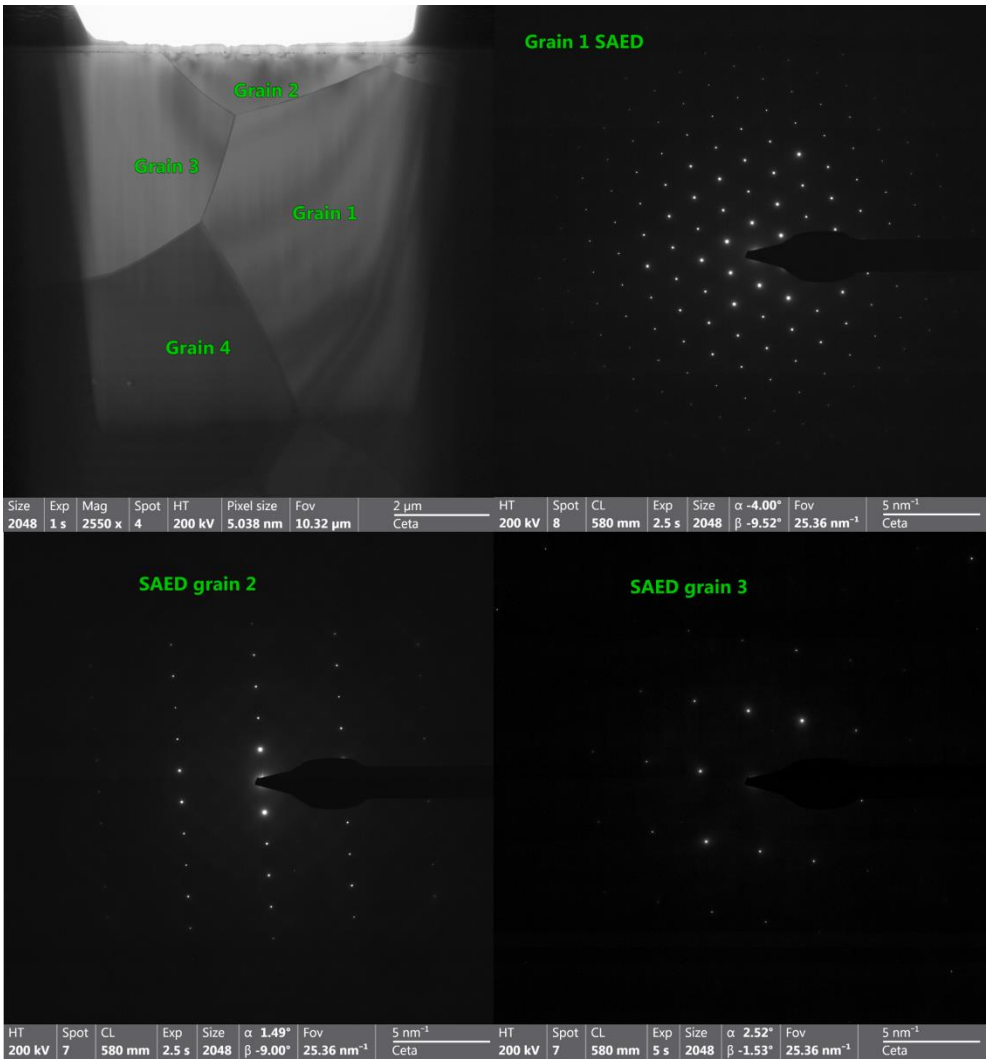

Figure 13 SAED of all four grains from TEM cross section study of vendor 1 ceramic.

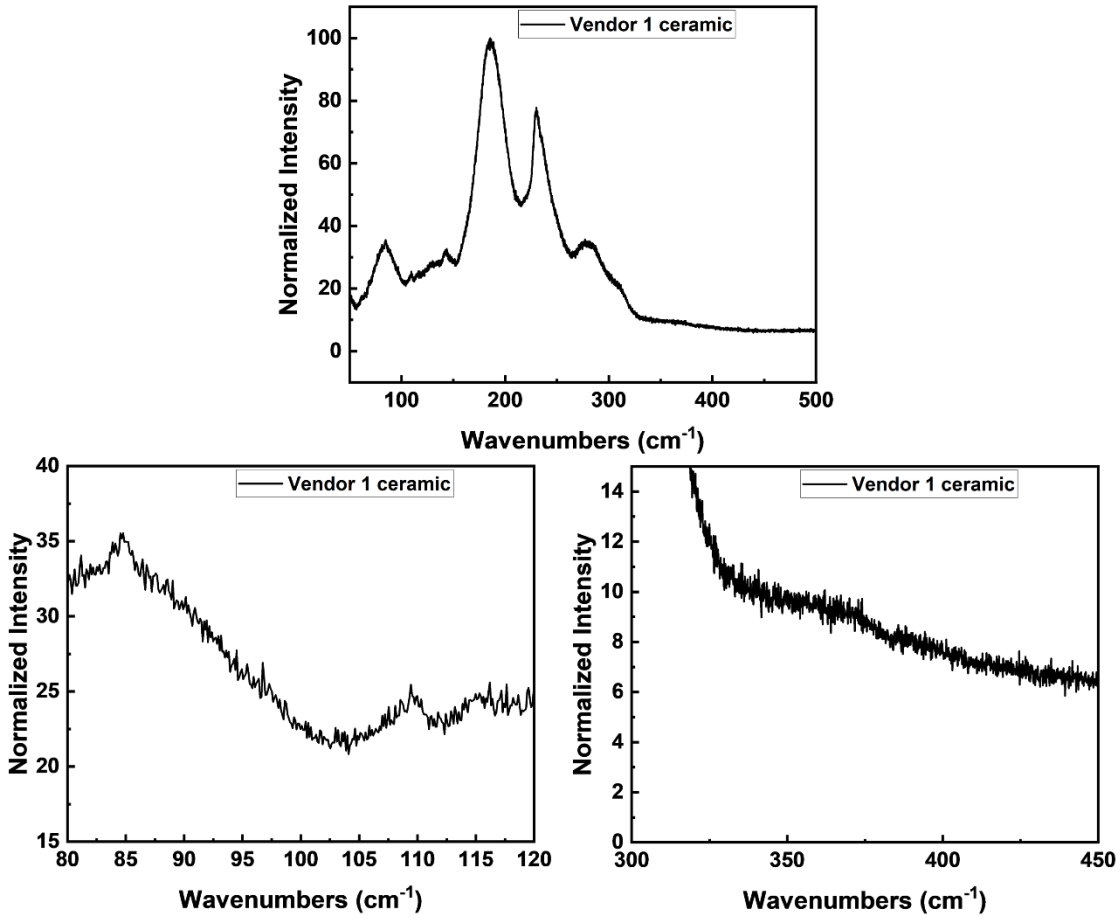

Figure 14 Raman spectrum of the vendor 1 ceramic from 50 - 500 cm^{-1} (top) and spectral regions between 80 - 120 cm^{-1} and 300 - 450 cm^{-1} that show the Raman mode associated with the La-O local vibrational modes.

LIST OF REFERENCES

1. Savage, J. and K. Marsh. *A Materials Study To Find An Advanced Optical Window Material For 8 to 12 pm Airborne Applications*. in *Emerging optical materials*. 1982. SPIE.
2. Goldstein, A. and A. Krell, *Transparent ceramics at 50: progress made and further prospects.* Journal of the American Ceramic Society, 2016. **99**(10): p. 3173-3197.
3. Zachariasen, W., *Crystal chemical studies of the 5f-series of elements. I. New structure types.* Acta Crystallographica, 1948. **1**(5): p. 265-268.
4. Zachariasen, W., *Crystal chemical studies of the 5f-series of elements. VI. The Ce2S3–Ce3S4 type of structure.* Acta Crystallographica, 1949. **2**(1): p. 57-60.
5. Bozorth, R., F. Holtzberg, and S. Methfessel, *Superconducting lanthanum chalcogenides.* Physical Review Letters, 1965. **14**(23): p. 952.
6. Batouche, M., et al., *Structural, electronic, optical and elastic properties of XLa2S4 (X= Ba; Ca): Ab initio study.* Physica B: Condensed Matter, 2019. **558**: p. 91-99.
7. Eastman, E., et al., *Preparation and Properties of Refractory Cerium Sulfides1a.* Journal of the American Chemical Society, 1950. **72**(5): p. 2248-2250.
8. Beswick, J., et al. *New infra-red window materials*. in *New Optical Materials*. 1983. SPIE.
9. Flahaut, J., et al., *Phase cubiques type Th3P4 dans les sulfures, les séléniures et les tellurures L2X3 et L3X4 des terres rares, et dans leurs combinaisons ML2X4 avec les sulfures et séléniures MX de calcium, strontium et baryum. Formation et propriétés cristallines.* Acta Crystallographica, 1965. **19**(1): p. 14-19.
10. Durand, G.R., et al., *Processing of CaLa2S4 infrared transparent ceramics: A comparative study of HP and FAST/SPS techniques.* Journal of the American Ceramic Society, 2020. **103**(4): p. 2328-2339.
11. Luguev, S., N. Lugueva, and S.M. Ismailov, *The Debye temperature and Grüneisen parameter of the CaLa 2 S 4-La 2 S 3 system.* Physics of the Solid State, 2002. **44**: p. 1067-1070.

12. Carter, F., R. Miller, and F. Ryan, *Considerations concerning thermoelectric materials having the thorium phosphide structure.* Advanced Energy Conversion, 1961. **1**: p. 165-175.

13. Gadzhiev, G.G., et al., *Thermophysical properties of sulfides of lanthanum, praseodymium, gadolinium, and dysprosium.* High Temperature, 2000. **38**: p. 875-879.

14. Lowe-Ma, C., *Characterization of rare earth sulfides.* Advances in Materials Characterization, 1983: p. 267-279.

15. Tsay, B.J. and L.H. Wang, *A study on infrared transmission of lanthanum sulfide and oxysulfide in the 2.5–14 μm region.* Materials Letters, 1998. **34**(3-6): p. 180-183.

16. Durand, G., *Élaboration de céramiques transparentes de $CaLa_2S_4$ pour applications optiques dans l'infrarouge*. 2017, Rennes 1.

17. Besançon, P., *Teneur en oxygéne et formule exacte d'une famille de composés habituellement appelés "variété β" ou "phase complexe" des sulfures de terres rares.* Journal of Solid State Chemistry, 1973. **7**(2): p. 232-240.

18. Saunders, K., et al. *Current and future development of calcium lanthanum sulfide*. in *Infrared and Optical Transmitting Materials*. 1986. SPIE.

19. Kumta, P.N. and S.H. Risbud, *Chemical processing of rare earth chalcogenides.* Progress in crystal growth and characterization of materials, 1991. **22**(4): p. 321-383.

20. Tsai, M.S. and M.H. Hon, *HOT-PRESS SINTERING AND THE PROPERTIES OF LANTHANUM-RICH CALCIUM LANTHANUM SULFIDE CERAMIC.* Journal of Materials Research, 1994. **9**(11): p. 2939-2943.

21. Vaughan, C.M. and W.B. White, *Role of Oxygen in Rare Earth Chalcogenide Semiconductors.* MRS Online Proceedings Library (OPL), 1987. **97**.

22. White, W.B., et al. *CaLa2S4: ceramic window material for the 8 to 14 pm region*. in *Emerging optical materials*. 1982. SPIE.

23. Shyam S. Bayya, W.K., Jasbinder S. Sanghera, Guillermo R. Villalobos, Ishwar D. Aggarwal, *Calcium lanthanoid sulfide powders, methods of making, and ceramic bodies formed therefrom*, U.S. Patent, Editor. 2017, The United States of America: United States. p. 13.

24. Tsay, B.J., L.H. Wang, and M.H. Hon, *Formation and densification of CaLa2S4 powders by sulfidization of modified metal alkoxides in different atmospheres.* Materials Science and Engineering B-Solid State Materials for Advanced Technology, 2000. **72**(1): p. 31-35.

25. LECO, *ONH 836*. 3000 Lakeview Ave, St. Joseph, MI 49085.

26. Horiba, *LabRAM HR Evolution*. 2 Miyanohigashi-cho, Kisshoin, Minami-ku, Kyoto, 601-8510, Japan.

27. *Thermo Fischer Scientific ESCALAB QXi X-ray Photoelectron Spectrometer Microprobe*. 168 Third Ave Waltham, MA USA 02451.

28. Butkus, B., et al., *Zinc sulfide chemical vapor deposition optical ceramic analyzed by XPS.* Surface Science Spectra, 2023. **30**(2).

29. Butkus, B., et al., *Lanthanum sulfide powder analyzed by XPS.* Surface Science Spectra, 2023. **30**(1).

30. Butkus, B., et al., *Calcium sulfide powder analyzed by XPS.* Surface Science Spectra, 2023. **30**(1): p. 014005.

31. *OxyGon FR730-150T-14X12-G-G-200-06D*. 2 Old Rte 28 N, Epsom, NH 03234.

32. Cullity, B. and S. Stock, *Elements of X-Ray Diffraction 3rd ed*. 2014, Pearson Education Limited.

33. Shannon, R.T. and C.T. Prewitt, *Effective ionic radii in oxides and fluorides.* Acta Crystallographica Section B: Structural Crystallography and Crystal Chemistry, 1969. **25**(5): p. 925-946.

34. Mauricot, R., et al., *Comparative study of some rare earth sulfides: doped γ-[A] M2S3 (M= La, Ce and Nd, A= Na, K and Ca) and undoped γ-M2S3 (M= La, Ce and Nd).* Journal of alloys and compounds, 1995. **223**(1): p. 130-138.

35. Eastman, E., et al., *Preparation and Properties of the Oxide-Sulfides of Cerium, Zirconium, Thorium and Uranium2.* Journal of the American Chemical Society, 1951. **73**(8): p. 3896-3898.

36. Appel, J. and S. Kurnick, *Polaron Band Model and Its Application to Ce–S Semiconductors.* Journal of Applied Physics, 1961. **32**(10): p. 2206-2210.

37. Havel, M., et al., *Monitoring sulfur loss in polycrystalline solid solutions of CaS-La 2 S 3 by Raman spectroscopy and X-ray diffraction.* Optical Materials Express, 2023. **13**(2): p. 504-513.

38. Lewis, K., et al., *Recent developments in the fabrication of rare-earth chalcogenide materials for infra-red optical applications.* New Optical Materials, 1983. **400**: p. 21-28.

39. Nakamoto, K., *Infrared and Raman spectra of inorganic and coordination compounds, part B: applications in coordination, organometallic, and bioinorganic chemistry*. 2009: John Wiley & Sons.

40. Chastain, J. and R.C. King Jr, *Handbook of X-ray photoelectron spectroscopy.* Perkin-Elmer Corporation, 1992. **40**: p. 221.

41. Le Coz, A., et al., *First La2O2S infrared transparent ceramics.* Journal of the European Ceramic Society, 2023. **43**(5): p. 2133-2142.

42. Merzbacher, C.I., D.L. Chess, and W.B. White, *Infrared optical properties of calcium lanthanum sulfide.* Materials Letters, 2010. **64**(3): p. 334-336.

43. May, A.F., E. Flage-Larsen, and G.J. Snyder, *Electron and phonon scattering in the high-temperature thermoelectric La 3 Te 4− z M z (M= Sb, Bi).* Physical Review B, 2010. **81**(12): p. 125205.

44. Nishibuchi, G.M., et al., *Electronic, mechanical, and vibrational properties of calcium lanthanum sulfide solid solution: A DFT study.* Journal of Applied Physics, 2023. **134**(17).